

14. Prah, F. G. & Carpenter, R. Hydrocarbons in Washington coastal sediments. *Estuar. Coast. Shelf Sci.* **18**, 703–720 (1984).

15. Vogel, J. S., Nelson, D. E. & Southon, J. R. C-14 background levels in an Accelerator Mass Spectrometry system. *Radiocarbon* **29**, 323–333 (1987).

16. Stuiver, M. & Polach, H. A. Reporting of <sup>14</sup>C data. *Radiocarbon* **19**, 355–363 (1977).

17. Wakeham, S. G. *et al.* Hydrocarbons in Lake Washington sediments: a 25-year retrospective in an urban lake. *Environ. Sci. Technol.* (in the press).

18. Wakeham, S. G., Lee, C., Hedges, J. I., Hernes, P. J. & Peterson, M. L. Molecular indicators of diagenetic status in marine organic matter. *Geochim. Cosmochim. Acta* **61**, 5363–5369 (1997).

19. Eglinton, T. I. *et al.* Composition, age and provenance of organic matter in NW African dust over the Atlantic Ocean. *Geochem. Geophys. Geosyst.* **3**, 1–27 (2002).

20. Weis, P. L. The origin of epigenetic graphite: evidence from isotopes. *Geochim. Cosmochim. Acta* **45**, 2325–2332 (1981).

21. Schidlowski, M. Carbon isotopes as biogeochemical recorders of life over 3.8 Ga of Earth history: evolution of a concept. *Precamb. Res.* **106**, 117–134 (2001).

22. Petsch, S. T., Smernik, R. J., Eglinton, T. I. & Oades, J. M. A solid-state <sup>13</sup>C-NMR study of kerogen degradation during black shale weathering. *Geochim. Cosmochim. Acta* **65**, 1867–1882 (2001).

23. Herring, J. R. in *The Carbon Cycle and Atmospheric CO<sub>2</sub>: Natural Variations, Archean to Present* (eds Sundquist, E. T. & Broecker, W. S.) 419–442 (AGU, Washington, 1985).

24. Suman, D. O., Kuhlbusch, T. A. J. & Lim, B. in *Sediment Records of Biomass Burning and Global Change* (ed. Clark, J. S.) 271–293 (Springer, Berlin, 1997).

25. Sackett, W. M., Poag, C. W. & Eadie, B. J. Kerogen recycling in the Ross Sea, Antarctica. *Science* **185**, 1045–1047 (1974).

26. Blair, N. E. *et al.* The persistence of memory: the fate of ancient sedimentary organic carbon in a modern sedimentary system. *Geochim. Cosmochim. Acta* **67**, 63–73 (2003).

27. Eglinton, T. I. *et al.* Variability in radiocarbon ages of individual organic compounds from marine sediments. *Science* **277**, 796–799 (1997).

28. Petsch, S. T., Berner, R. A. & Eglinton, T. I. A field study of the chemical weathering of ancient sedimentary organic matter. *Org. Geochem.* **31**, 475–487 (2000).

29. Jahnke, R. A. The global ocean flux of particulate organic carbon: Areal distribution and magnitude. *Glob. Biogeochem. Cycles* **10**, 71–88 (1996).

30. Druffel, E. R. M., Williams, P. M., Livingston, H. D. & Koide, M. Variability of natural and bomb-produced radionuclide distributions in abyssal red clay sediments. *Earth Planet. Sci. Lett.* **71**, 205–214 (1984).

Supplementary Information accompanies the paper on [www.nature.com/nature](http://www.nature.com/nature).

**Acknowledgements** We thank the scientific staff at the Lawrence Livermore National Laboratory Center for Accelerator Mass Spectrometry for assistance with radiocarbon analyses, C. Preston and C. Swanston for radiocarbon analysis of the Stillaguamish River sample, S. Petsch and R. Smernik for providing kerogen samples for analysis, and P. Quay and E. Druffel for editing and comments. This work was supported by a mini-grant from LLNL CAMS and by grants from the NSF; A.E.D. thanks the NSF for a graduate research fellowship; Y.G. thanks the Canadian NSERC and Quebec NATEQ for support for this work.

**Competing interests statement** The authors declare that they have no competing financial interests.

**Correspondence** and requests for materials should be addressed to A.D. ([dickensa@u.washington.edu](mailto:dickensa@u.washington.edu)).

## Melting of iron at the physical conditions of the Earth's core

Jeffrey H. Nguyen & Neil C. Holmes

Physics and Advanced Technologies, H-Division, Lawrence Livermore National Laboratory, Livermore, California 94551, USA

Seismological data can yield physical properties of the Earth's core, such as its size and seismic anisotropy<sup>1–3</sup>. A well-constrained iron phase diagram, however, is essential to determine the temperatures at core boundaries and the crystal structure of the solid inner core. To date, the iron phase diagram at high pressure has been investigated experimentally through both laser-heated diamond-anvil cell and shock-compression techniques, as well as through theoretical calculations<sup>4–17</sup>. Despite these contributions, a consensus on the melt line or the high-pressure, high-temperature phase of iron is lacking. Here we report new and re-analysed sound velocity measurements of shock-compressed iron at Earth-core conditions<sup>15</sup>. We show that melting starts at  $225 \pm 3$  GPa ( $5,100 \pm 500$  K) and is complete at

$260 \pm 3$  GPa ( $6,100 \pm 500$  K), both on the Hugoniot curve—the locus of shock-compressed states. This new melting pressure is lower than previously reported<sup>16</sup>, and we find no evidence for a previously reported solid–solid phase transition on the Hugoniot curve near 200 GPa (ref. 16).

The radii of the solid inner core and the molten outer core are roughly 1,220 km (pressure  $P = 329$  GPa)<sup>1</sup> and 3,490 km ( $P = 136$  GPa), respectively. About 20 years ago, Brown and McQueen reported iron melting at 243 GPa (ref. 16). This has since been the high pressure ‘anchor’ of the iron melt line (Fig. 1). Their proposed solid–solid transition has also driven the search for a solid–solid phase boundary near 200 GPa (refs 4–8). At different times, the  $\gamma$ – $\epsilon$  (ref. 4) and  $\beta$ – $\epsilon$  (ref. 5) phase boundaries were proposed to explain this solid–solid transition (Fig. 1). However, recent data placed the liquid– $\gamma$ – $\epsilon$  triple point between 50 and 60 GPa (refs 6–8). The  $\beta$ – $\epsilon$  phase boundary has been shown to be nearly horizontal, that is, no intersection with the melt curve at 200 GPa (refs 7, 8) (Fig. 1). The existence of the  $\beta$ -phase is also questionable<sup>6,9</sup>. Thus there is at present no other experimental evidence consistent with the putative solid–solid phase transition reported by Brown and McQueen<sup>16</sup>.

To corroborate their sound velocity data<sup>16</sup>, we focused our experiments between 200 and 260 GPa, employing similar but improved sound velocity measurement techniques<sup>15</sup>. Longitudinal sound velocity ( $C_L$ ), commonly used to determine melting of metals at high pressures<sup>15–21</sup>, decreases sharply on melting. In a solid,  $C_L$  depends on bulk and shear moduli and density, whereas it is only a function of the bulk modulus and density in a liquid. Upon melting, the shear modulus of the solid–liquid mixture tends to zero causing sound velocity to decrease. In metals such as Ta, Al and Mo,  $C_L$  decreases by 5–15% when the Hugoniot crosses the melt curve<sup>18–21</sup>.

We carried out these experiments using a two-stage gas gun capable of generating pressures as high as 400 GPa in the iron sample. This pressure exceeds that at the centre of the Earth, 361 GPa, making single shock experiments suitable for exploring

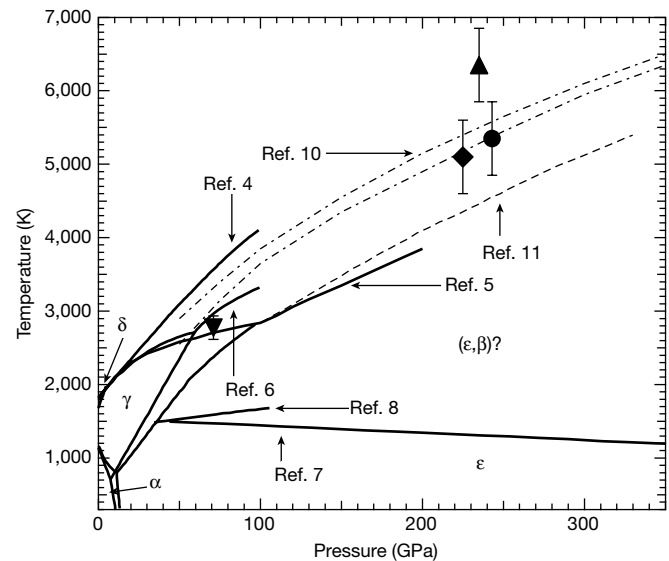


**Figure 1** Iron phase diagram. Solid lines, phase boundaries and melt lines from DAC experiments<sup>4–8</sup>. For clarity, uncertainties of the melt curve, often hundreds of degrees, are not included here. Dashed curve, calculated melt curve by Laio *et al.*<sup>11</sup>. Upper (lower) dash-dotted curve, calculation with (without) free energy correction by Alfè *et al.*<sup>10</sup>. Data points are taken from shock-compression experiments. Triangle data point is from pyrometric temperature measurement by Yoo *et al.*<sup>9</sup>. Circle (Brown and McQueen<sup>16</sup>), reverse triangle (Ahrens *et al.*<sup>17</sup>) and diamond (this study) data points are from sound velocity experiments. Temperatures of these sound velocity data points are calculated using thermodynamic relations (equation (4)).

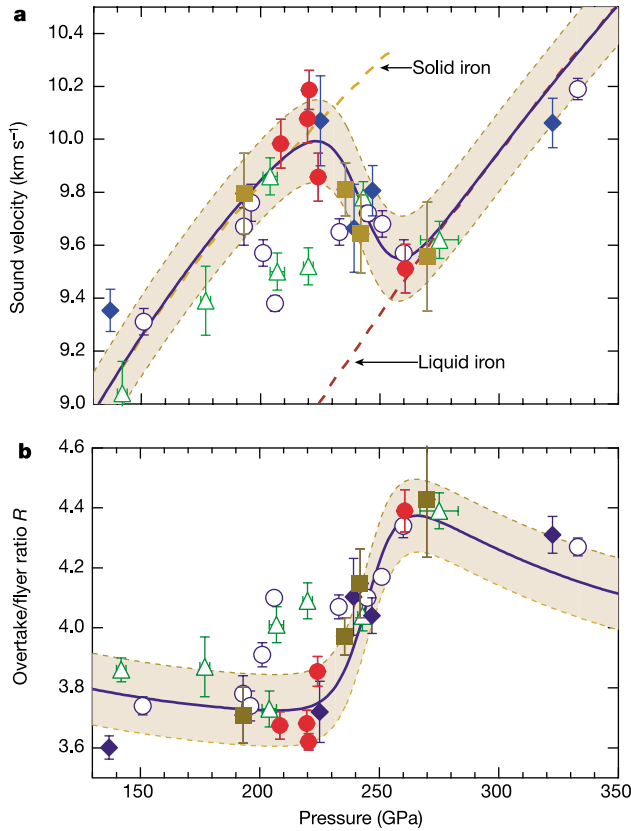


**Figure 2** Sound velocity and overtake ratio. **a**, Sound velocity from this study (solid symbols) exhibits a single solid–liquid transition along the Hugoniot at  $225 \pm 3$  GPa. The solid circles (squares, diamonds) represent sample number 1 (2, 3) (see Table 1). Brown and McQueen’s<sup>16</sup> data are shown by open symbols. The open circles (triangles) represent gas gun (explosive driven) shock data. The heavy-dashed lines are calculated sound velocities<sup>16</sup>. The solid line is a fit to data from this study using equation (2), and the area within the dashed lines is its associated  $1\sigma$  prediction band. **b**, Overtake ratio of sample plate thickness to impactor plate thickness. This ratio, which is a direct experimental measurement, clearly shows a simple transition. Data are fitted to an equation for  $R$ , which is analogous to equation (2).  $C_L$ ,  $C_s$  and  $C_{\text{liquid}}$  are replaced by  $R$ ,  $R_s$  and  $R_{\text{liquid}}$ . The latter terms are inverted from the former using equation (1).

core conditions. Just as important, the principal Hugoniot of iron crosses the melt line at a pressure between those of the core–mantle boundary and the inner–outer core boundary. In these single shock experiments, the impact generates two planar shock fronts travelling at shock velocity  $U_s$  in opposite directions: one forward into the iron sample, the other backward into the iron impactor. The latter reflects forward, at the back end of the impactor, as a rarefaction wave moving at longitudinal sound velocity  $C_L$ . As  $C_L + U_p > U_s$  (for a rarefaction wave propagating in shocked material moving at particle velocity  $U_p$ )<sup>22</sup>, the rarefaction wave eventually overtakes the forward-moving shock wave  $U_s$ .

As iron is opaque, we measured these overtake events indirectly after the shock and rarefaction fronts have left the iron sample. We designed sample plates with up to seven steps on the non-impact side, and filled the volume behind the stepped surface with bromoform. Above 20 GPa shock pressure, bromoform becomes opaque and emits light whose intensity varies roughly as  $U_p^8$ . This intensity decreases as the rarefaction wave overtakes the shock front ( $U_p$  decreases). These two events (shock break-out and rarefaction overtake) define the overtake time. By extrapolating the overtake times to zero, we determined the minimum iron thickness (overtake distance) necessary for an overtake event to take place in iron. Overtake times are a linear function of step thicknesses<sup>23</sup>. From the

Table 1 Trace-element concentrations and initial densities

	Sample 1	Sample 2	Sample 3	Ref. 16
C	0.04	0.03		0.02
Al	0.0092	0.0450		
Si	<0.005	0.0060		0.1
P	0.0080	0.0180		
S		0.007		
V	<0.0005	0.0756		
Cr	0.0083	0.0182		
Mn	0.0004	0.3440		0.7
Co	0.0025	0.0039		
Ni	0.0019	0.0148		
Cu	0.0066	0.0040		
$\rho_o$ (g cm <sup>-3</sup> )	7.870(3)	7.817(4)	7.859(4)	7.850

Trace element analysis was done by Elemental Research Inc., using laser ablation mass spectroscopy. Carbon analysis was done by LECO, Inc. Nitrogen, oxygen and sulphur trace concentrations were not measured. Sulphur concentration was supplied by the manufacturer. No analysis was done for sample no. 3. Sample densities were measured by the volume displacement method (immersion density). The value in the parentheses represents the uncertainty of the last significant digit.

ratio ( $R$ ) of overtake distance to impactor thickness (Fig. 2b), we calculated the longitudinal sound velocity as<sup>16</sup>:

$$C_L = \left(\frac{\rho_o}{\rho}\right) U_s \frac{(R+1)}{(R-1)} \quad (1)$$

where  $\rho_o$  and  $\rho$  are the ambient and shocked iron densities, respectively. The shocked sample density and velocity,  $\rho$  and  $U_s$ , are calculated from  $\rho_o$  (Table 1) and  $U_p$ , using the Hugoniot and conservation relations<sup>16,22</sup>. In symmetric experiments (iron impactors), particle velocity  $U_p$  is exactly one-half that of the impactor velocity<sup>22</sup>. To make a simple and direct comparison with Brown and McQueen’s<sup>16</sup> sound velocity data, we used the same linear fit to the Hugoniot data that they used,  $U_s = c + sU_p$  where  $c = 3.955 \pm 0.028$  km s<sup>-1</sup> and  $s = 1.580 \pm 0.011$  (ref. 16). Calculations with their recently revised iron Hugoniot data<sup>24</sup> do not affect the measurement of the onset of melting.

Our sound velocity data are in good agreement with that of Brown and McQueen<sup>16</sup>, except between 200 GPa and 243 GPa (Fig. 2a). Within this pressure range, we observed a monotonic decrease in  $C_L$  and a similar increase in  $R$  starting at  $225 \pm 3$  GPa (Fig. 2). In order to discern the number of phase transitions (decreasing steps in sound velocity), we employed two different models: a single solid–liquid phase transition model (equation (2)), and a two-phase transitions model (equation (3)),

$$C_L = [f(P, P_c, \omega)C_\omega] + [(1 - f(P, P_c, \omega))C_{\text{liquid}}] \quad (2)$$

$$C_L = [f(P, P_{c1}, \omega_1)C_\epsilon] + [(1 - f(P, P_{c1}, \omega_1))f(P, P_{c2}, \omega_2) C_\beta] + [(1 - f(P, P_{c2}, \omega_2))C_{\text{liquid}}] \quad (3)$$

where  $f(P, P_c, \omega) = \{1 + \exp[-(P - P_c)/\omega]\}^{-1}$ .  $C_\epsilon$ ,  $C_\beta$  and  $C_{\text{liquid}}$  are calculated sound velocities for the two proposed solid phases and a liquid phase, respectively<sup>16</sup>.  $f(P, P_c, \omega)$  is a smoothly varying connecting function of pressure,  $P$ , with centre at  $P_c$  and width  $\omega$ ;  $P_c$  and  $\omega$  are used as fitting parameters.  $C_\epsilon$ ,  $C_\beta$  and  $C_{\text{liquid}}$  are treated as ‘constants’ without affecting reduced  $\chi^2$ .

The two-phase transition equation (equation (3)) fits well to Brown and McQueen’s data<sup>16</sup> (Table 2). Reduced  $\chi^2$  results suggest that both models can describe our data (Table 2). However, on closer examination, contribution from the  $C_\beta$  line (second term, equation (3)) seems unconstrained, resulting in an abnormally large  $1\sigma$  prediction band. On the other hand, the prediction band from equation (2) encompassed approximately 68.3% of our data, as expected (Fig. 2a). From these observations, we conclude that equation (2)—the one phase transition model—sufficiently describes our data. The existence of another solid phase is thus not discernible from our data. This interpretation is consistent with those of Al and Ta<sup>19–21</sup>.

Table 2 Fitting parameters and reduced  $\chi^2$

	Equation (2)	Equation (3)	Ref. 16 (equation (3))
Reduced $\chi^2$	2.68	2.44	4.15
$\rho_{c1}$	$243.5 \pm 2.1$	$224.4 \pm 1.1$	$201.7 \pm 0.8$
$\omega_1$	$7.2 \pm 1.8$	$1.4 \pm 2.0$	$2.6 \pm 0.6$
$\rho_{c2}$		$252.7 \pm 4.3$	$252.4 \pm 1.5$
$\omega_2$		$7.2 \pm 2.4$	$5.4 \pm 1.2$

Fitting parameters and reduced  $\chi^2$  from equations (2) and (3). Reduced  $\chi^2$  is defined as  $\chi^2/(N - m)$  where  $N$  and  $m$  are the numbers of data points and parameters, respectively. For comparison purposes, we fit equation (3) to Brown and McQueen's<sup>16</sup> data in the same pressure range (190 and 275 GPa). Fitting to the entire set of data yields a slightly larger reduced  $\chi^2$ , but no significant changes in the fitting parameters.

In Fig. 2a, we segregated our sound velocity data by sample initial densities and concentrations of trace elements (Table 1). Whether taken separately or together, data from all three samples indicate the existence of one single phase transition. Slight differences in sample purity did not affect sound velocity in our study. Whether differences in sound velocity between our samples and those of Brown and McQueen<sup>16</sup> can be attributed to sample purity is not obvious.

Consistent with previous sound velocity studies, we define the onset of melting at the intersection of  $C_e$  and the linear extrapolation of the fitted sound velocity at  $P_c$  (refs 16, 19–21). We infer from our data a single solid–liquid phase transition starting at  $225 \pm 3$  GPa and completing at  $260 \pm 3$  GPa. The sound velocity decreases by 6% and the pressure range of the solid–melt region extends for  $35 \pm 4$  GPa from  $225 \pm 3$  to  $260 \pm 3$  GPa. This is twice the previous 3% decrease in sound velocity and the  $17 \pm 3$  GPa pressure range for the solid–liquid regime of Brown and McQueen<sup>16</sup>. However, this sound velocity decrease falls within range of those of 2024 Al, Mo and Ta (6–14%)<sup>18–20</sup>. Our Hugoniot pressure range of the mixed region is between those of 2024 Al, Mo and Ta (15–30 GPa)<sup>18–20</sup> and that of iron (65 GPa)<sup>13</sup>. Thus our interpretation of a single phase transition is consistent with other similar studies<sup>18–20</sup>.

Temperatures were not measured in these experiments. Instead, they are calculated by integrating the thermodynamic relation,

$$dT = -(T\gamma/V)dV + [(V_o - V)dP + (P - P_o)dV]/(2C_V) \quad (4)$$

along the Hugoniot<sup>16</sup>. Accurate temperature calculation requires accurate values of the Grüneisen parameter  $\gamma$  and heat capacity  $C_V$ . Only estimates are available; for comparison purposes, we used the same values used by Brown and McQueen<sup>16</sup>. Interpolation of their calculations yields a melting temperature of  $5,100 \pm 500$  K at 225 GPa, the melting pressure. Wasserman *et al.*'s<sup>25</sup> calculations of temperature on the iron Hugoniot, with temperature as a fitting parameter, are also in good agreement with those of Brown and McQueen<sup>16</sup> within cited uncertainty. Interpolation of their calculation yields a temperature of  $\sim 5,300$  K at 225 GPa.

Even though our new melting pressure at  $225 \pm 3$  GPa is significantly lower than the previously reported  $243 \pm 2$  GPa (ref. 16), the two calculated temperatures are on approximately the same melt curve (Fig. 1). This was due to the correction for entropy of solid–solid transition at 200 GPa which lowers their melting temperature by roughly 350 K (ref. 16); there was no such correction in our calculation. Our new calculated melting temperature is about  $1,000 \pm 700$  K lower than the measured temperature of shock-melted iron<sup>13</sup>, and is higher than the highest measured diamond-anvil cell (DAC) result<sup>5</sup> by about  $1,000 \pm 540$  K. In general, our result falls in between simple extrapolations of DAC melting curves<sup>4–6</sup>, but assessing uncertainties associated with extrapolation over such a large pressure range is beyond the scope of this work. Calculations by Alfè *et al.*<sup>10</sup>, within uncertainties of experiments, match well with sound velocity measurements: this study, Brown and McQueen's<sup>16</sup> and Ahrens *et al.*<sup>17</sup>. Laio *et al.*'s<sup>11</sup> calculations are more in line with Boehler's DAC results<sup>5</sup>.

Superheating in shock compression experiments has been

observed in non-metals<sup>26</sup>. However, superheating alone cannot explain the temperature discrepancies between shock and static measurements of melting of transition metals at  $P > 100$  GPa (ref. 27). Experimentally, there is no superheating in aluminium<sup>28</sup>, and evidence is statistically insignificant in iron<sup>13</sup>. This can in part be explained by the fast relaxation times ( $\leq 10^{-12}$  s) for electron–electron, electron–phonon and phonon–phonon thermalization in metals<sup>29</sup>. This fast relaxation time allows equilibrium to be quickly established in shocked metals.

Our observation of no solid–solid phase transition is consistent with both the proposed nearly-horizontal  $\beta$ – $\epsilon$  phase boundary<sup>7,8</sup> and the finding of no  $\beta$ -Fe (ref. 6; Fig. 1). Unfortunately, our experimental pressure range does not cross this new  $\beta$ – $\epsilon$  phase boundary and we cannot discern the crystal structure of iron with sound velocity. Nevertheless, existence of a solid–solid phase transition near 200 GPa as previously reported<sup>16</sup> is not consistent with these recent studies<sup>6–8</sup>—but our finding is consistent.

Using the pure iron melt line to study the temperature of the Earth's core is neither simple nor direct. The Earth's solid inner core is predominantly iron, but available data suggest the possible presence of oxygen and sulphur among others in the liquid outer core. However, with an understanding of eutectic melting depression in the Fe–FeO–FeS system<sup>30</sup> at core pressures, we can obtain sufficient estimates for temperature at the core boundaries. □

Received 4 April; accepted 25 November 2003; doi:10.1038/nature02248.

- Lehmann, I. P. *Publ. Bur. Cent. Seismol. Int.* **A 14**, 87–115 (1936).
- Song, X. & Richards, P. G. Seismological evidence for differential rotation of the Earth's inner core. *Nature* **382**, 221–224 (1996).
- Su, W., Dziewonski, A. M. & Jeanloz, R. Planet within a planet: rotation of the inner core of Earth. *Science* **274**, 1883–1887 (1996).
- Williams, Q., Jeanloz, R., Bass, J., Svendsen, B. & Ahrens, T. J. The melting curve of iron to 250 gigapascals: a constraint on the temperature at Earth's center. *Science* **236**, 181–182 (1987).
- Boehler, R. Temperatures in the Earth's core from melting-point measurements of iron at high static pressures. *Nature* **363**, 534–536 (1993).
- Shen, G., Mao, H. K., Hemley, R. J., Duffy, T. S. & Rivers, M. L. Melting and crystal structure of iron at high pressures and temperatures. *Geophys. Res. Lett.* **25**, 373–376 (1998).
- Saxena, S. K. & Dubrovinsky, L. S. Iron phases at high pressures and temperatures: phase transition and melting. *Am. Mineral.* **85**, 372–375 (2000).
- Andraut, D., Fiquet, G., Charpin, T. & Le Bihan, T. Structure analysis and stability field of  $\beta$ -iron at high pressure and temperature. *Am. Mineral.* **85**, 364–371 (2000).
- Yoo, C. S., Akella, J., Campbell, A. J., Mao, H. K. & Hemley, R. J. Phase diagram of iron by in situ x-ray diffraction: implications for Earth's core. *Science* **270**, 1473–1475 (1995).
- Alfè, D., Price, G. D. & Gillan, M. J. Iron under Earth's core conditions: Liquid-state thermodynamics and high-pressure melting curve from ab initio calculations. *Phys. Rev. B* **65**, 165118 (2002).
- Laio, A., Bernard, S., Chiarotti, G. L., Scandolo, S. & Tosatti, E. Physics of iron at Earth's core conditions. *Science* **287**, 1027–1030 (2000).
- Ahrens, T. J., Bass, J. D. & Abelson, J. R. in *Shock Compression of Condensed Matter—1989* (eds Schmidt, S. C., Johnson, L. W. & Davison, L. W.) (Elsevier Science, Amsterdam, 1990).
- Yoo, C. S., Holmes, N. C., Ross, M., Webb, D. J. & Pike, C. Shock temperatures and melting of iron at Earth core conditions. *Phys. Rev. Lett.* **70**, 3931–3934 (1993).
- Benuzzi-Mounaix, A. *et al.* Absolute equation of state measurements of iron using laser driven shocks. *Phys. Plasma* **9**, 2466–2469 (2002).
- Nguyen, J. H. & Holmes, N. C. in *Shock Compression of Condensed Matter—1999* (eds Furnish, M. D., Chhabildas, L. C. & Hixson, R. S.) 81–84 (American Institute of Physics, New York, 1999).
- Brown, J. M. & McQueen, R. G. Phase transitions, Grüneisen parameter, and elasticity for shocked iron between 77 GPa and 400 GPa. *J. Geophys. Res.* **91**, 7485–7494 (1986).
- Ahrens, T. J., Holland, K. G. & Chen, C. Q. Phase diagram of iron, revised-core temperatures. *Geophys. Res. Lett.* **29**, 54–1–54–4 (2002).
- Hixson, R. S., Boness, D. A., Shane, J. W. & Moriarty, J. A. Acoustic velocities and phase transitions in molybdenum under strong shock compression. *Phys. Rev. Lett.* **62**, 637–640 (1989).
- Brown, J. M. & Shaner, J. W. in *Shock Compression of Condensed Matter—1983* (eds Asay, J. R., Graham, R. A. & Straub, G. K.) 91–94 (North-Holland, Amsterdam, 1984).
- McQueen, R. G., Fritz, J. N. & Morris, C. E. in *Shock Compression of Condensed Matter—1983* (eds Asay, J. R., Graham, R. A. & Straub, G. K.) 95–98 (North-Holland, Amsterdam, 1984).
- Shaner, J. W., Brown, J. M. & McQueen, R. G. Melting of metals above 100 GPa. *Mater. Res. Soc. Symp. Proc.* **22**, 137–141 (1984).
- Zel'dovich, Y. B. & Raizer, Y. P. *Physics of Shock Waves and High-Temperature Hydrodynamic Phenomena* (Academic, New York, 1967).
- McQueen, R. G., Hopson, J. W. & Fritz, J. N. Optical technique for determining rarefaction wave velocities at very high pressures. *Rev. Sci. Instrum.* **53**, 245–250 (1982).
- Brown, J. M., Fritz, J. N. & Hixson, R. S. Hugoniot data for iron. *J. Appl. Phys.* **88**, 5496–5498 (2000).
- Wasserman, E., Stixrud, L. & Cohen, R. E. Thermal properties of iron at high pressures and temperatures. *Phys. Rev. B* **53**, 8296–8309 (1996).
- Lou, S. N. & Ahrens, T. J. Superheating systematics of crystalline solids. *Appl. Phys. Lett.* **82**, 1836–1838 (2003).
- Lou, S. N. & Ahrens, T. J. Application of shock-induced superheating to the melting of geophysically important minerals. *Phys. Earth Planet. Inter.* (in the press).

28. Boehler, R. & Ross, M. Melting curve of aluminum in a diamond cell to 0.8 Mbar: implications for iron. *Earth Planet. Sci. Lett.* **153**, 223–227 (1997).
29. Wallace, D. C. Irreversible thermodynamics of flow in solids. *Phys. Rev. B* **22**, 1477–1486 (1980).
30. Boehler, R. Melting of the Fe-FeO and Fe-FeS systems at high-pressure—constraints on core temperatures. *Earth Planet. Sci. Lett.* **111**, 217–227 (1992).

**Acknowledgements** We benefited from discussions with J. M. Brown, O. L. Anderson, M. Ross and R. Boehler. We acknowledge F. H. Streitz for the formulation of equations (2) and (3). We are grateful for the technical efforts of S. Caldwell, E. Ojala, L. Raper, K. Stickle. Work was performed by the University of California under the auspices of the US DOE by the Lawrence Livermore National Laboratory.

**Competing interests statement** The authors declare that they have no competing financial interests.

**Correspondence** and requests for materials should be addressed to J.H.N. (nguyen29@llnl.gov).

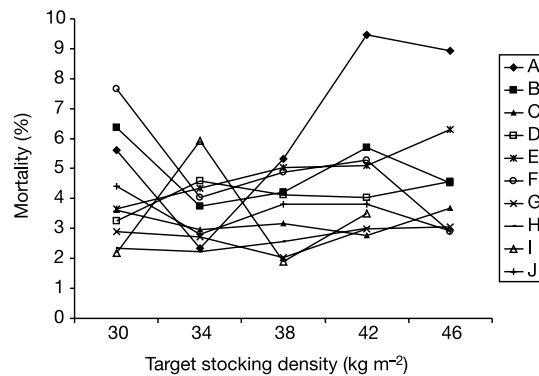


**Figure 1** Total mortality in relation to target stocking density. The percentage of total mortality is shown separately for each company (A–J) taking part in the trial.

## Chicken welfare is influenced more by housing conditions than by stocking density

Marian Stamp Dawkins, Christi A. Donnelly\* & Tracey A. Jones

Department of Zoology, University of Oxford, South Parks Road, Oxford OX1 3PS, UK

\* Present address: Department of Infectious Disease Epidemiology, Faculty of Medicine, Imperial College London, St. Mary's Campus, Norfolk Place, London W2 1PB, UK

**Intensive broiler (meat) chicken production now exceeds 800 million birds each year in the United Kingdom and  $2 \times 10^{10}$  birds worldwide<sup>1</sup>, but it attracts accusations of poor welfare<sup>2,3</sup>. The European Union is currently adopting standards for broilers aimed at a chief welfare concern—namely, overcrowding—by limiting maximum ‘stocking density’ (bird weight per unit area). It is not clear, however, whether this will genuinely improve bird welfare because evidence is contradictory<sup>4–10</sup>. Here we report on broiler welfare in relation to the European Union proposals through a large-scale study (2.7 million birds) with the unprecedented cooperation of ten major broiler producers in an experimental manipulation of stocking density under a range of commercial conditions. Producer companies stocked birds to five different final densities, but otherwise followed company practice, which we recorded in addition to temperature, humidity, litter and air quality. We assessed welfare through mortality, physiology, behaviour and health, with an emphasis on leg health and walking ability. Our results show that differences among producers in the environment that they provide for chickens have more impact on welfare than has stocking density itself.**

Across companies, there was a wide range of house sizes (455–1,901 m<sup>2</sup>), house ages (5–40 yr) and numbers of birds per house (7,500–53,000); 75% of flocks were Ross 308 (see Supplementary Information). Each company contributed two houses to each target stocking density for a trial. With two companies, we repeated trials with the same ten houses in summer and winter to examine the effects of season. Within a company, houses were randomly assigned to stocking density (Supplementary Information), which was manipulated by altering the numbers of day-old chicks placed to achieve a projected ‘target’ maximum stocking density just before the birds were killed (39–42 d at 2–3 kg). The five target stocking densities were 30, 34, 38, 42 and 46 kg m<sup>-2</sup> (refs 1, 11, 12). Actual stocking density was measured as mean weight  $\times$  number of birds per area of house. The same person (T.A.J.) made or checked all measurements with the help of trained assistants.

Welfare<sup>13–15</sup> was assessed through mortality, physiology, behaviour and health, emphasizing leg health and walking ability<sup>16–20</sup> (Table 1). We found that the effect of experimentally manipulating stocking density was overshadowed by much larger differences among companies (Table 2 and Fig. 1). Chickens grew more slowly at the highest stocking densities and jostled each other more, and fewer of them showed the best gaits (Table 3); however, for the most obvious measures of bird welfare—that is, the numbers of birds dying, being culled as unfit and showing leg defects—there was no effect of stocking density. There were, however, substantial differences among companies in almost all measures examined (Table 2). At no point was breed a significant explanatory factor in any outcome variables, suggesting that the differences were due to environmental influences.

Of the commercially relevant factors that seemed to allow some companies to ‘cope’ better than others with high stocking densities, the most likely candidates were those that affected litter moisture

Table 1 Scoring of gait, hockburn, pad dermatitis and leg deviations

Leg health measure	Score 0	Score 1	Score 2
Gait	Bird walks with ease, has regular and even strides and is well balanced	Bird walks with irregular and uneven strides and appears unbalanced	Bird is reluctant to move and is unable to walk many strides before sitting down
Hockburn*	No discolouration or lesions	<10% hock with lesion	>10% hock with lesion
Pad dermatitis†	No lesions	<5 mm lesion on pad	>5 mm lesion on pad
Angle: in	Legs straight	Inward bow at intertarsal joint so that the two legs meet >22°	
Angle: out	Legs straight	Outward twist at intertarsal joint with $\geq 30^\circ$ between the legs	
Rotation	Legs straight, pads facing away from handler	Rotation of the tibia shaft so that pads face each other >15°	

\* Pink hocks were also recorded.

† Pervasively dirty pads also scored.